J Solid State Electrochem (2010) 14:1657–1666
DOI 10.1007/s10008-010-1008-x

ORIGINAL PAPER

Solid-state synthesis and characterization of Ca-substituted $YAlO_3$ as electrolyte for solid oxide fuel cells

Ramya Hariharan · A. Venkatasubramanian · Prakash Gopalan

Received: 29 August 2009 / Revised: 7 January 2010 / Accepted: 13 January 2010 / Published online: 9 February 2010

Abstract ABO_3-type oxides are recently being explored as solid electrolytes for solid oxide fuel cells. The objective of this work was to study an ABO_3-type perovskite oxide, $YAlO_3$, for its electrical properties and its suitability as a solid electrolyte. The undoped and doped compositions of $Y_{1-x}Ca_xAlO_{3-\delta}(x = 0 - 0.25)$ have been synthesized. The phase purity of the samples has been investigated by X-ray diffraction studies. The electrical conductivity studies have been performed using ac impedance spectroscopy in the range 200–800 °C in air. The doped $YAlO_3$ compositions exhibit a total conductivity of about 1 mS/cm at 800 °C. The microstructural evaluation of the samples has been conducted by scanning electron microscopy and energy dispersive spectrum analysis.

Keywords ABO_3-type oxides · Solid oxide fuel cells · Yttrium aluminate · Electrical conductivity

Introduction

ABO_3-type oxides form an important class of materials of great technical value in several applications. Such oxides are known to exist with a wide range of A and B ions. Most of these oxides have the relatively simple structure of the mineral perovskite ($CaTiO_3$) [1]. The ideal perovskite structure has a cubic unit cell. However, distortions are common and depend upon the value of the tolerance factor [2]. Rhombohedral structure or orthorhombic $GdFeO_3$-type structure is found when the tolerance factor is less than unity [3]. Polytypic structures are observed when the tolerance factor is greater than unity. Other structures such as ilmenite and pyrochlore also occur [4]. ABO_3-type oxides display a wide spectrum of physical properties of technical importance such as ferroelectricity, antiferroelectricity, piezoelectricity, insulating behavior, semi-conductivity, metallic conductivity, superconductivity, ferromagnetism, antiferromagnetism, etc. [5]. The ferroelectric properties are mostly controlled by the relative sizes of the ions. The electrical and magnetic properties are mainly dependent on the electronic configuration of the ions. Dopants and substituents have a profound influence on the properties of the ABO_3 oxides.

Generally, ABO_3 oxides are electronic conductors. Ionic conduction is not favored because of the close-packed nature of the perovskite structure. However, it has recently been found that substitution in some ABO_3 oxides can lead to ionic conduction. Substitution by lower valence ions of fixed valency within the solubility limit at the cation site in these ABO_3 oxides creates oxygen vacancies for charge neutrality. An increase in the oxygen ionic conduction owing to the hopping of oxide ions through the vacancies is observed. These oxide ion conductors find applications as electrolytes in solid oxide fuel cells (SOFCs) [6–11]. In some ABO_3 oxides, wet atmospheric conditions at elevated temperatures lead to the generation of protonic carriers by incorporation of water vapor. These proton-conducting oxides also serve as electrolytes in SOFCs [12–17].

For perovskite oxides to behave as solid electrolytes, the following considerations are to be made [18]. The cations introduced into perovskite A and B lattice sites must be devoid of multiple oxidation states so as to avoid electronic transport via this mechanism. The perovskite crystallographic lattice must possess a relatively open structure or free volume facilitating ionic mobility. The aliovalent

R. Hariharan · A. Venkatasubramanian · P. Gopalan (✉)
Department of Metallurgical Engineering and Materials Science,
Indian Institute of Technology, Bombay,
Powai, Mumbai 400 076, India
e-mail: pgopalan@iitb.ac.in

dopant cation introduced into the A or B lattice site for creation of oxygen vacancies that are necessary for promoting ionic conduction must possess an ionic radius similar to the host cation. In the case of oxide ion conductors, the saddle point critical radius ($r_{critical}$) formed by two A and one B lattice site, through which mobile anions must pass, has to be large enough so that minimal disturbance of the lattice occurs. The inherent band gap between valence and conduction bands within the perovskite solid electrolyte must be large enough to suppress parasitic electronic conductivity.

Numerous studies have been devoted to investigate the ionic conductivities of the perovskites based on doped cerates and zirconates; Y-, Sc-, or Yb-doped $SrCeO_3$ being among the first systems investigated for protonic conduction [19–21]. Gd-, Sm-, or Y-doped $BaCeO_3$ oxides have been reported to exhibit considerable protonic conduction at high temperatures [22–25]. Sr- or Ca-doped $BaZrO_3$ and Gd-doped $BaPrO_3$ are some of the other ABO_3-type perovskites exhibiting protonic conduction [26–28]. ABO_3-type perovskites with the rare earth elements for A-site cations and elements like Al, Ga, In, Sc, and Y for B-site cations are being studied. Lanthanum is the element among the rare earth elements giving the highest conductivity as an A-site ion [29]. $LaGaO_3$-based perovskite-type oxides have been shown to exhibit extremely high oxide ion conductivity [30, 31]. Doped $LaGaO_3$ materials are promising oxide ionic conductors, with conductivity values higher than that of the fluorite-type ZrO_2- or CeO_2-based materials. However, doped $LaGaO_3$ does not exhibit protonic conduction [12]. Doped $LaScO_3$ is a mixed conductor exhibiting p-type electronic conduction at high oxygen partial pressures and ionic conduction at low oxygen partial pressures. The ionic conductivity contains both proton and oxide ion contributions at low pO_2 [32, 33]. Doped $LaInO_3$ is also a mixed p-type and ionic conductor that is unstable in reducing atmospheres [34]. $LaErO_3$ has been reported to exhibit protonic conductivity [12].

There have been a number of studies on the ionic conductivity of perovskite aluminate-based systems [35–41]. Acceptor-doped perovskite aluminates such as $LnAlO_3$ [42] have attracted significant interest since the 1970s. Their advantages include relatively low cost and moderate thermal expansion as compared to doped $CeO_{2-\delta}$. When Ca ions are added on the A-site of $LnAlO_3$, the following defect reaction occurs:

$$2CaO + Al_2O_3 \rightarrow 2Ca'_{Ln} + 2Al^x_{Al} + 5O^x_O + V^{\bullet\bullet}_O.$$

From the above equation, it is understood that as more divalent cations are introduced, within the solubility limit, the concentration of oxygen vacancies increases. The electrical properties of $LaAlO_3$ have been investigated by several researchers using conductivity and electromotive force (EMF) measurements [43]. Kilner et al. [44] used EMF measurements to show that the ionic transport number of $La_{0.9}Ca_{0.1}AlO_{2.95}$ is unity between 10^{-8} and 10^{-12} atm O_2 (g). These results indicate that doped $LaAlO_3$ may be a useful electrolyte at low oxygen partial pressures [45, 46]. It is found that $Nd_{0.9}Ca_{0.1}AlO_{2.95}$ exhibits p-type electronic conduction at higher partial pressures and oxygen ion conduction at lower partial pressures [47]. Also, Zn-substituted $SmAlO_3$ exhibits a mixed ionic and p-type conduction [48]. $GdAlO_3$ is a new family of perovskite fast ion conductor, and the electrical conductivity of 15% calcium substitution at A-site has been reported to be 0.057 S/cm at 1,000 °C [49]. To summarize, the orthoaluminate families are stable and are of relatively low cost. But they exhibit certain limitation in terms of low oxide ion conductivity, relatively high p-type electronic transport under oxidizing conditions, and poor sinterability.

Yttrium aluminate is one of the materials which have been widely investigated for its good optical properties, and it is a very promising lasing material [50]. $YAlO_3$ is an excellent material for gain media, scintillators, and acousto-optics. Its crystal structure varies between hexagonal and orthorhombic depending on the temperature. In $YAlO_3$, an ABO_3-type perovskite, Y^{3+} ions are positioned on the A-site in eightfold coordination, while the Al^{3+} ions are present on the B-site in sixfold coordination. The tolerance factor, which is a relation between the ionic radius of the A and B site cation, of the material is about 0.9. The A- and B-site cations, namely, Y and Al, have stable oxidation states. Hence, it is a promising candidate as an electrolyte for SOFC applications. Moreover, the starting materials are of relatively low cost [51, 52].

In the present study, we report the synthesis and electrical properties of undoped and Ca-doped $YAlO_3$ system. The structural and microstructural evaluation has been carried out by X-ray diffraction and scanning electron microscopy.

Experimental section

The Ca-doped $YAlO_3$ samples were prepared by the solid-state route. As the undoped $YAlO_3$ samples offered very poor sinterability, only those samples were prepared by chemical route.

Synthesis of undoped yttrium aluminate powder

Undoped yttrium aluminate powder was prepared by the citrate gel route. The starting materials taken were $Y(NO_3)_3{\cdot}5H_2O$ (Aldrich, 99.99% pure) and $Al(NO_3)_3{\cdot}9H_2O$ (Aldrich, 99.99+% pure). The precursor solution was prepared by dissolving the required amount of metal

nitrates in distilled water. A calculated amount of citric acid was added to the solution: 1 mol of trivalent cations needed 1 mol of citric acid. Twice the amount of citric acid to metal cations in distilled water was added dropwise to the prepared aqueous solution to chelate Y^{3+} and Al^{3+} cations in the solution. The solution was continuously stirred for about 3–4 h at 80 °C until a brown gel was obtained. The gel was dried in an oven at about 130 °C for 4 h. The dried resin was charred in a furnace at 400 °C for 1 h to obtain the dried precursor. The precursor powder was calcined at 1,100 °C for 2 h. A subsequent 24 h ball milling in polyethylene jar containing zirconia balls in ethanol was performed to break the soft agglomerates and mix the powders to homogeneity. The calcined powders were then uniaxially cold-pressed at 30 kg/cm^2 for 60 s into a 10 mm diameter pellet. The pressed pellets were sintered at 1,575 °C for 12 h. Heating rate was 5 °C/min, and the sample was cooled at 5 °C/min until 800 °C and then furnace-cooled to room temperature.

Synthesis of Ca-doped yttrium aluminate powders

$Y_{1-x}Ca_xAlO_{3-\delta}(x = 0.03 - 0.25)$ was prepared by the conventional solid-state synthesis route. The starting materials taken were Y_2O_3 (Alfa Aesar, 99.99% pure), Al_2O_3 (Aldrich, 99.99+% pure), and $CaCO_3$ (Aldrich, 99.5% pure). Y_2O_3 was pre-calcined in the furnace for about 5 h at 1,000 °C to ensure the correct stoichiometry. Powders were weighed and mixed to homogeneity in polyethylene jar containing zirconia balls in ethanol for about 48 h to obtain the desired composition. A 1:2 weight ratio of powder to zirconia balls was used. The mixed powders were filtered, dried, and calcined at 1,200 °C for about 18 h. The calcined powders were subjected to ball milling again with zirconia balls in ethanol for 48 h to break the agglomerates. A 1:4 weight ratio of powder to zirconia balls was used this time to achieve a smaller particle size. These powders were uniaxially cold-pressed at 30 kg/cm^2 for 60 s into pellets of diameter 10 mm. Compositions with x between 0.03 and 0.12 were sintered for 12 h at 1575 °C. Compositions with x between 0.18 and 0.25 were sintered at 1,525 °C for 12 h. Heating rate for all cases was 5 °C/min, and all samples were furnace-cooled to room temperature. Density was calculated for the pellets from their geometry, and the relative density with respect to the theoretical density was estimated.

X-ray diffraction analysis

Phase distributions were studied by powder X-ray diffraction (XRD) analysis using Cu K_α radiation with 40-kV acceleration voltage and 30 mA filament current (X'Pert Pro, PANalytical). Scan rate of 0.01°/s was employed. Sample preparation for the analysis was performed by grinding the powders in an agate mortar. XRD analysis was performed for the fine-grained powder thus obtained by spreading the powder smoothly on a substrate.

Conductivity measurement using impedance spectroscopy

Impedance spectroscopy was used to measure frequency-dependent electrical impedance of the pellets. Bulk, grain boundary, and electrode impedances were identified. Pellets were polished up to 1,200 grit emery sheet to obtain a smooth and flat surface. Alfa Aesar platinum paste was applied on one side and dried at 100 °C to remove the

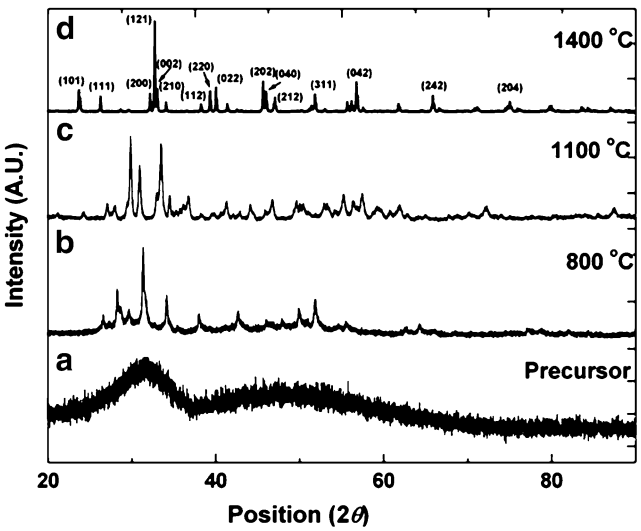

Fig. 1 Thermal evolution of the powder X-ray diffraction patterns of $YAlO_3$ powder

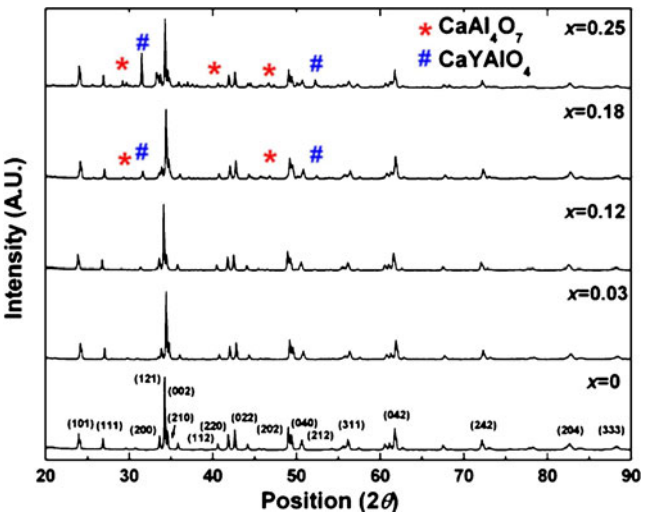

Fig. 2 XRD patterns of $Y_{1-x}Ca_xAlO_{3-\delta}$ powders (x=0–0.25) calcined at 1,400 °C for 6 h

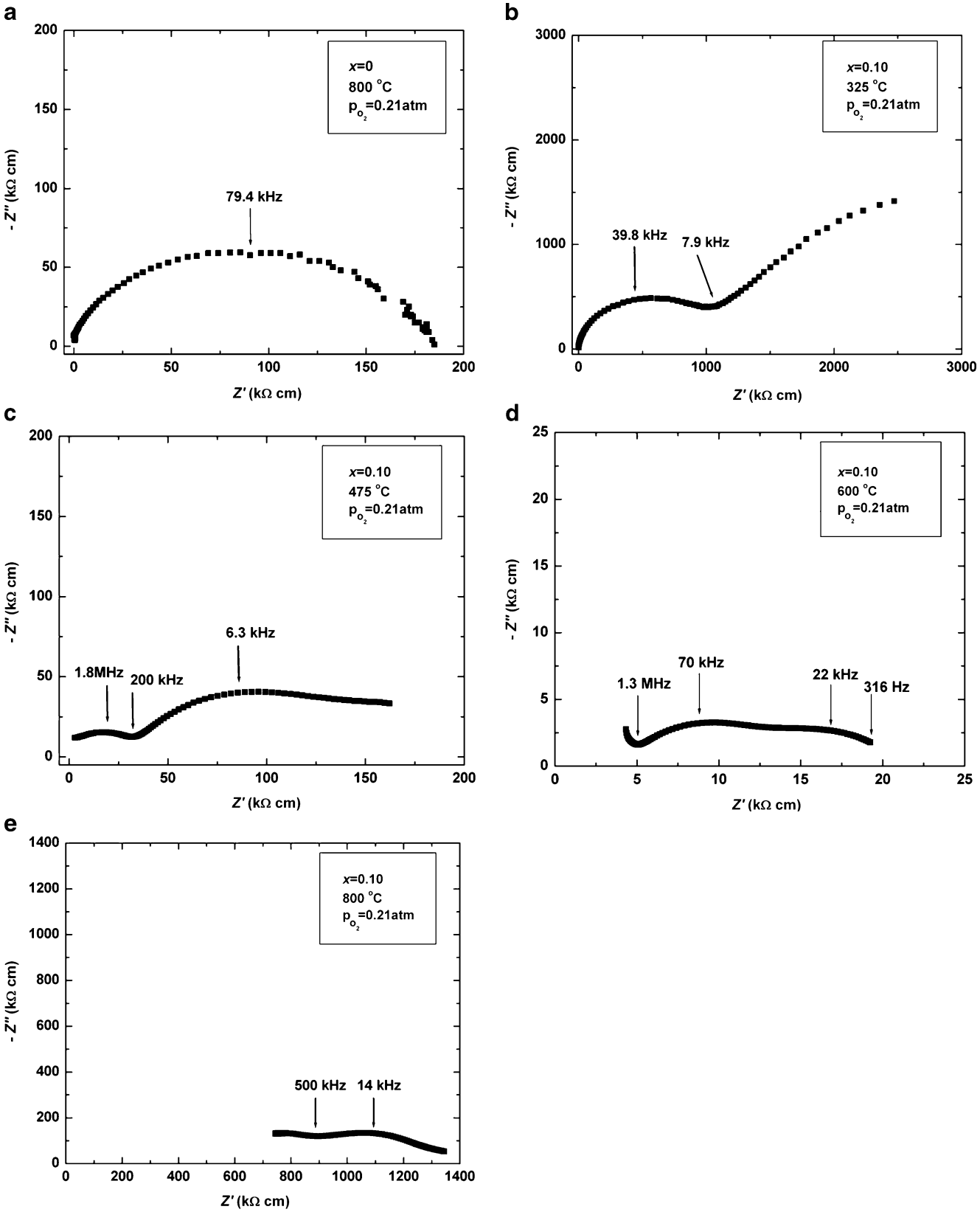

Fig. 3 Nyquist plots of undoped $YAlO_3$ at 800 °C in air and $Y_{0.9}Ca_{0.1}AlO_{3-\delta}$ sample at different temperatures in air

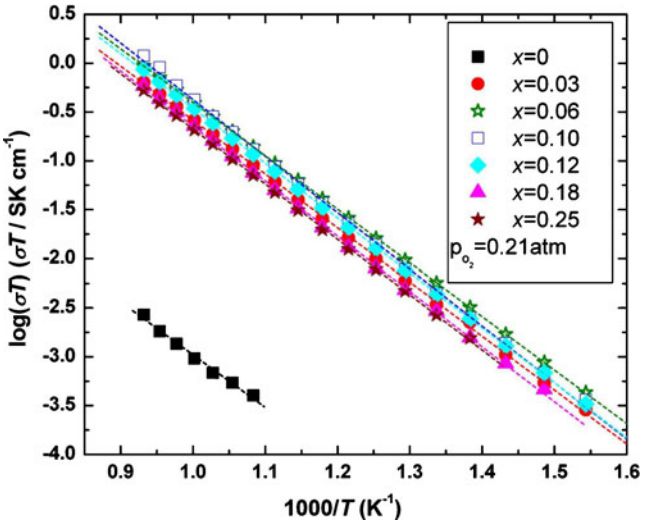

Fig. 4 Arrhenius plot of total conductivity of $Y_{1-x}Ca_xAlO_{3-\delta}$ samples (x=0–0.25)

organic content, then paste was applied on the other side. Platinum-coated pellets were fired at 1,100 °C for 2 h to have proper adhesion of Pt electrode with electrolyte. Heating and cooling rates were controlled at 5 °C/min. HP4192A impedance analyzer was used for recording the impedance data of the sample in the frequency range 100 Hz–13 MHz. PROBOSTAT™ sample holder (Norwegian Ceramic Society, Norway) was employed for all conductivity measurements. Heating and cooling rate of the furnace was controlled by a Eurotherm 2416 temperature controller. Impedance measurements were conducted in air (po_2=0.21 atm) with an applied potential of 1 V in the temperature range of 200–800 °C. Over this temperature range, the frequency response of the samples covered bulk, grain boundary, and electrode arcs.

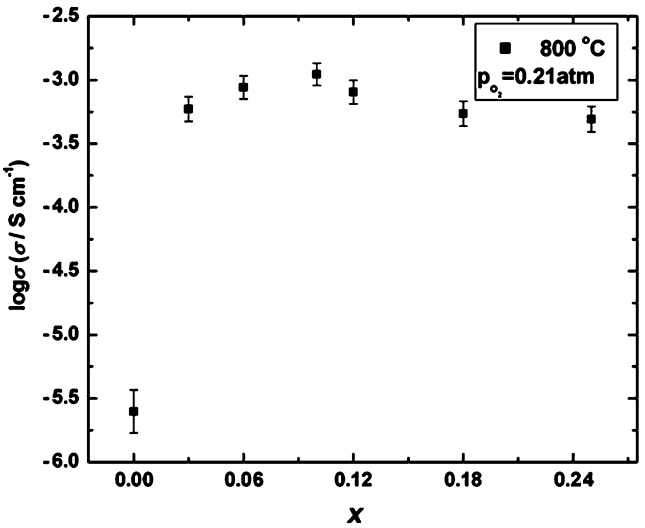

Fig. 5 Plot comparing total conductivity of $Y_{1-x}Ca_xAlO_{3-\delta}$ samples at 800 °C

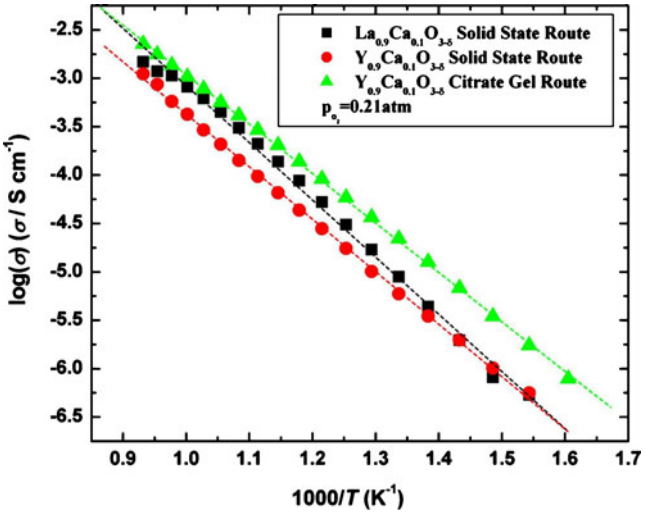

Fig. 6 Comparison of total conductivities of $La_{0.9}Ca_{0.1}AlO_{3-\delta}$ (solid-state route), $Y_{0.9}Ca_{0.1}AlO_{3-\delta}$ (citrate gel route), and $Y_{0.9}Ca_{0.1}AlO_{3-\delta}$ (solid-state route)

SEM/EDS analysis

The microstructures of the sintered pellets were obtained by the scanning electron microscopy coupled with energy-dispersive spectrum (SEM/EDS) technique. Hitachi S-3400N SEM (coupled with Thermo Noran EDS analyzer) was employed for the studies. The pellets were polished with various grades of emery sheets. The samples were thermally etched at 1,300 °C for 2 h.

Results and discussion

X-ray diffraction

The phase development in the undoped $YAlO_3$ powder prepared by citrate gel route has been closely examined by

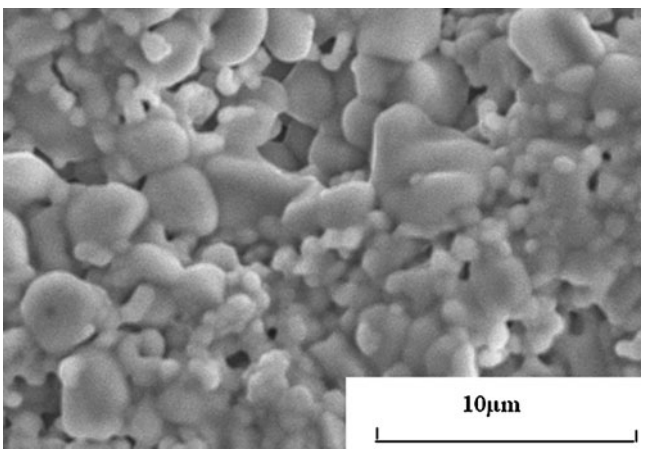

Fig. 7 SEM micrograph of $YAlO_3$ showing agglomerated grains

studying the XRD patterns in the temperature range 400–1,400 °C. Figure 1 shows the XRD patterns of $YAlO_3$ precursor powder calcined at different temperatures. The precursor powder as dried at 400 °C for 1 h shows high background counts without any reflections, indicating the amorphous nature of the powder. The pattern of the powder calcined at 800 °C for 2 h corresponds to the perovskite phase with traces of garnet and monoclinic phases. The hexagonal $YAlO_3$ phase is known to transform to the orthorhombic $YAlO_3$ phase at 1,100 °C [53]. The orthorhombic $YAlO_3$ phase is stable above 1,100 °C, and the pattern of the powder calcined at 1,400 °C for 6 h is in good agreement with those reported in the International Centre for Diffraction Data (ICDD) database (ICDD no.70-1677). It is also confirmed that the obtained compound is a single phase.

Although the perovskite-type phases in doped $YAlO_3$ systems were found to form at 1,200 °C, a higher calcination temperature, 1,400 °C for 6 h, was selected for XRD study to ensure complete crystallization of primary phase. It was also noted that an increase in the dopant concentration reduced the sintering temperature. The Ca-doped $YAlO_3$ samples showed higher sintered densities and lower sintering temperatures as compared to the undoped $YAlO_3$. The undoped $YAlO_3$ prepared by the solid-state route showed a relative density of about 60%, which was improved to about 70% by the chemical route of synthesis. There was a steep increase in the relative density with the addition of a few mole percents of Ca. The average relative density of the Ca-doped $YAlO_3$ pellets was about 85%. However, the densities of the samples prepared by this route were lower than of those that were prepared by the chemical route. The reason for this may be the higher calcination temperature, poor mixing, and reactivity of the powder synthesized by the solid-state route.

Figure 2 shows the diffraction patterns of selected compositions of $Y_{1-x}Ca_xAlO_{3-\delta}$ powders (x=0–0.25). Powder X-ray diffraction analysis confirmed that these compounds are single-phase perovskites with traces of secondary phases for x>0.12. The formation of a single phase clearly indicates that the Ca cation is substitutionally introduced into the Y site. The patterns could be indexed using

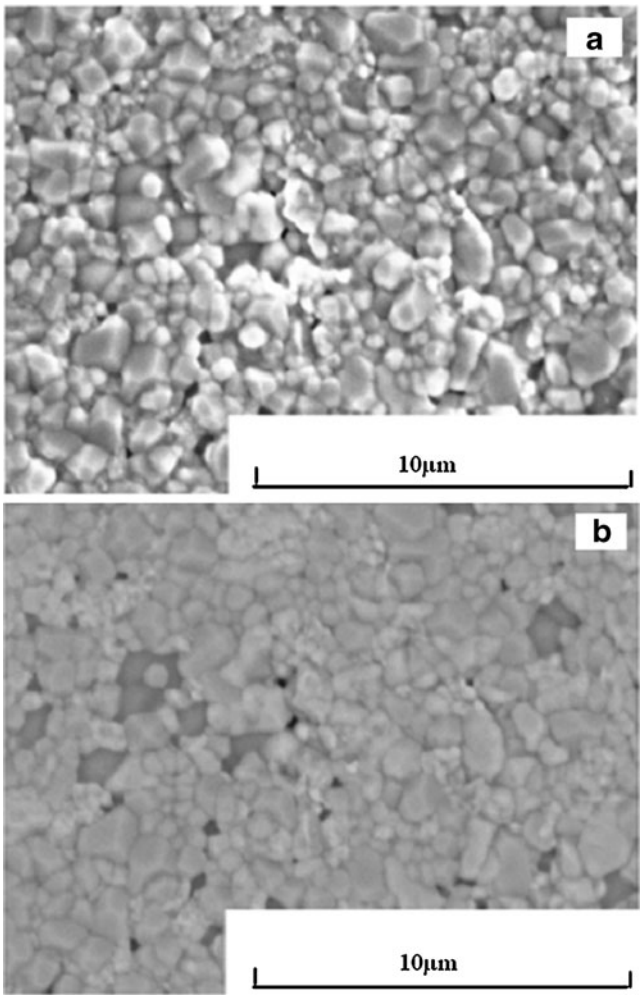

Fig. 8 SEM micrographs of $Y_{0.88}Ca_{0.12}AlO_{3-\delta}$ in secondary electron mode (**a**) and backscattered electron mode (**b**)

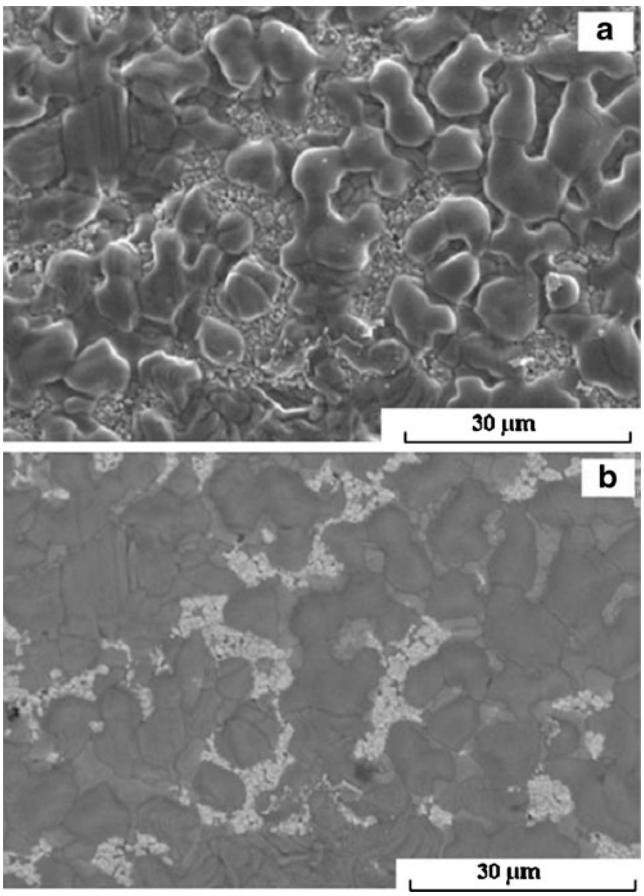

Fig. 9 SEM micrographs of $Y_{0.82}Ca_{0.18}AlO_{3-\delta}$ in secondary electron mode (**a**) and backscattered electron mode (**b**)

the orthorhombic space group Pnma known for the $GdFeO_3$ structure. The additional reflections for $x>0.12$ reveal the presence of secondary phases like $CaAl_4O_7$ (ICDD no.76–0706) and $CaYAlO_4$ (ICDD no.81-1588). This suggests that the solubility limit of CaO in $YAlO_3$ is $x=0.12$.

ac impedance spectroscopic studies

Figure 3a–e shows the Nyquist plots of undoped and 10% doped $YAlO_3$ sample. The Nyquist plot at 800 °C of undoped $YAlO_3$ is seen in Fig. 3a. Since these materials are polycrystalline in nature, arcs instead of semicircles are observed. Distinct arcs indicate relaxation frequencies of different processes that are well separated.

Figure 3b–e shows the Nyquist plots of $Y_{0.9}Ca_{0.1}AlO_{3-\delta}$ at different temperatures (300–800 °C) showing semicircular arcs representing different processes in the ionically conducting sample. At 325 °C, the semicircle corresponding to the bulk of the electrolyte is visible. At 475 °C, two distinct arcs are seen corresponding to the bulk and grain boundary components of the electrolyte as manifested in the capacitance values. A capacitance value in the picofarad range corresponds to the bulk region, and a capacitance in the nanofarad range corresponds to the grain boundary region of the electrolyte. As electrode reaction kinetics are sluggish, arc corresponding to electrode reaction is not visible at this temperature. As the temperature increases, relaxation frequency of bulk increases beyond the upper frequency limit of impedance analyzer, and hence, it slowly vanishes at high temperatures. Beyond 600 °C, the bulk arc completely merges into the grain boundary arc, and the resistance of the electrolyte is assigned by the total resistance. As the temperature increases, electrode reaction rate increases, and this process falls in the detectable limit of impedance analyzer with a capacitance value of about 10^{-8} F [54].

Effect of dopant content on the total conductivity

The obtained conductivity values are plotted against temperature in Fig. 4. Conductivity data obey the Arrhenius relation:

$$\sigma = (\sigma_o/T)\exp(-E_a/KT)(\mathrm{S/cm})$$

where σ_o, T, E_a, and K are the pre-exponential constant, absolute temperature, activation energy, and Boltzmann constant (8.617×10^{-5} eV/K), respectively. Undoped $YAlO_3$ specimen exhibited a total conductivity of 2.5×10^{-6} S/cm at 800 °C. The calculated activation energy for conduction for undoped $YAlO_3$ system is 1.08 eV. The calculated value

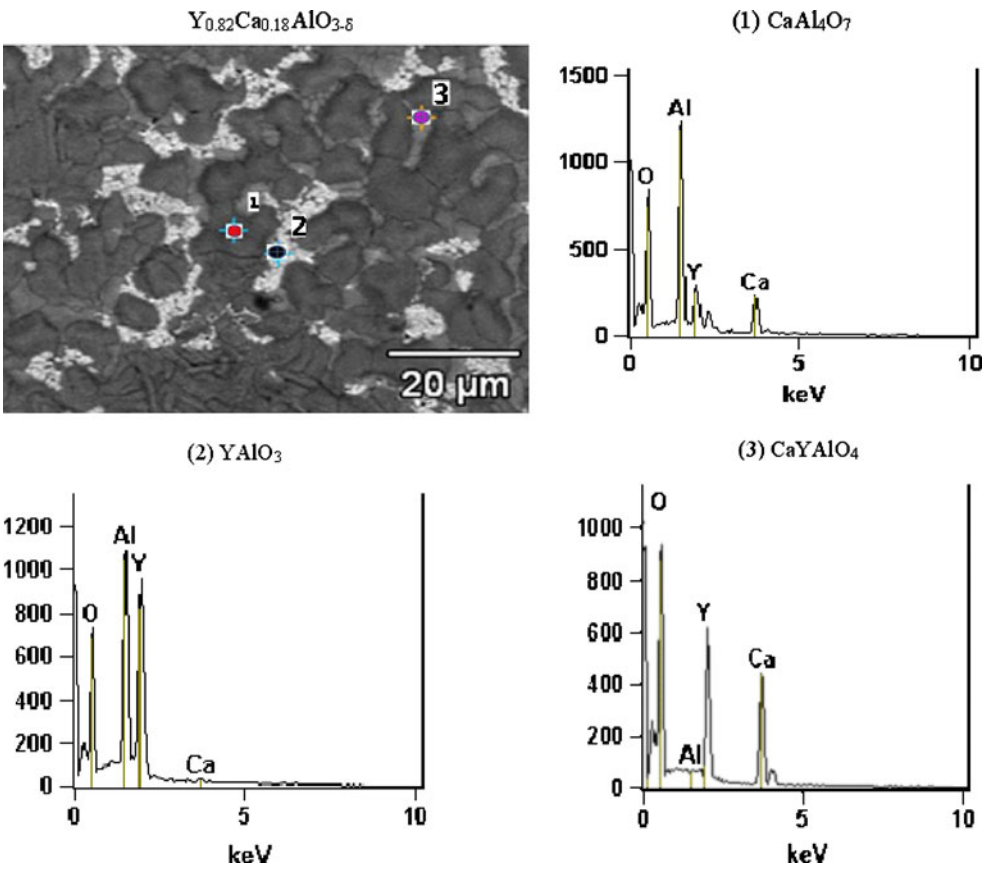

Fig. 10 EDS spectra along with backscattered electron image revealing the phases in the $Y_{0.82}Ca_{0.18}AlO_{3-\delta}$ sample

is comparable with the activation energies of rare earth aluminate systems reported in literature. The activation energy of undoped $LaAlO_3$ has been recorded to be about 1.3 eV, and that of $GdAlO_3$ has been documented to be about 1.4 eV [49, 55].

Even with a very small doping percentage of calcium, x= 0.03, the conductivity of the system increases by almost three orders of magnitude as compared to the undoped yttrium aluminate. Substitution by lower valence ions of fixed valency at the A or B site in ABO_3 oxides creates oxygen vacancies for charge neutrality. As a result, an increase in the oxygen ion conduction is observed. The improved conductivity in this case may be due to the creation of oxide ion vacancies when Y^{3+} ions are substituted by Ca^{2+} ions. Since the transport number has not been estimated, the conductivity measured for the doped $YAlO_3$ samples is the total conductivity. The increase in conductivity can also be attributed to the increase in cell volume of the perovskite that assists the mobility of oxygen ion. The increase in cell volume with calcium doping is the result of larger ionic radius of Ca^{2+} (1.12 Å) in eightfold coordination relative to that for Y^{3+} (1.019 Å) [56] in the same coordination. Figure 5 shows the conductivity of various samples at 800 °C as a function of Ca content. With increase in the Ca content, the conductivity steadily increases. When the doping level is x>0.10, the conductivity gradually falls.

Effect of preparation route on total conductivity

The maximum conductivity obtained is about 1 mS/cm at 800 °C. A comparison of the total conductivity of $Y_{0.9}Ca_{0.1}AlO_{3-\delta}$ sample synthesized by the traditional solid-state route, citrate gel route, and $La_{0.9}Ca_{0.1}AlO_{3-\delta}$ (LCA) is shown in Fig. 6. The Ca-doped yttrium aluminate system synthesized by the citrate gel route shows a slightly higher conductivity than the LCA sample and its solid-state counterpart. The advantage of chemical route of synthesis in achieving better homogeneity, smaller particle size, higher density, and hence an increased conductivity over the solid-state route is evident from the comparison.

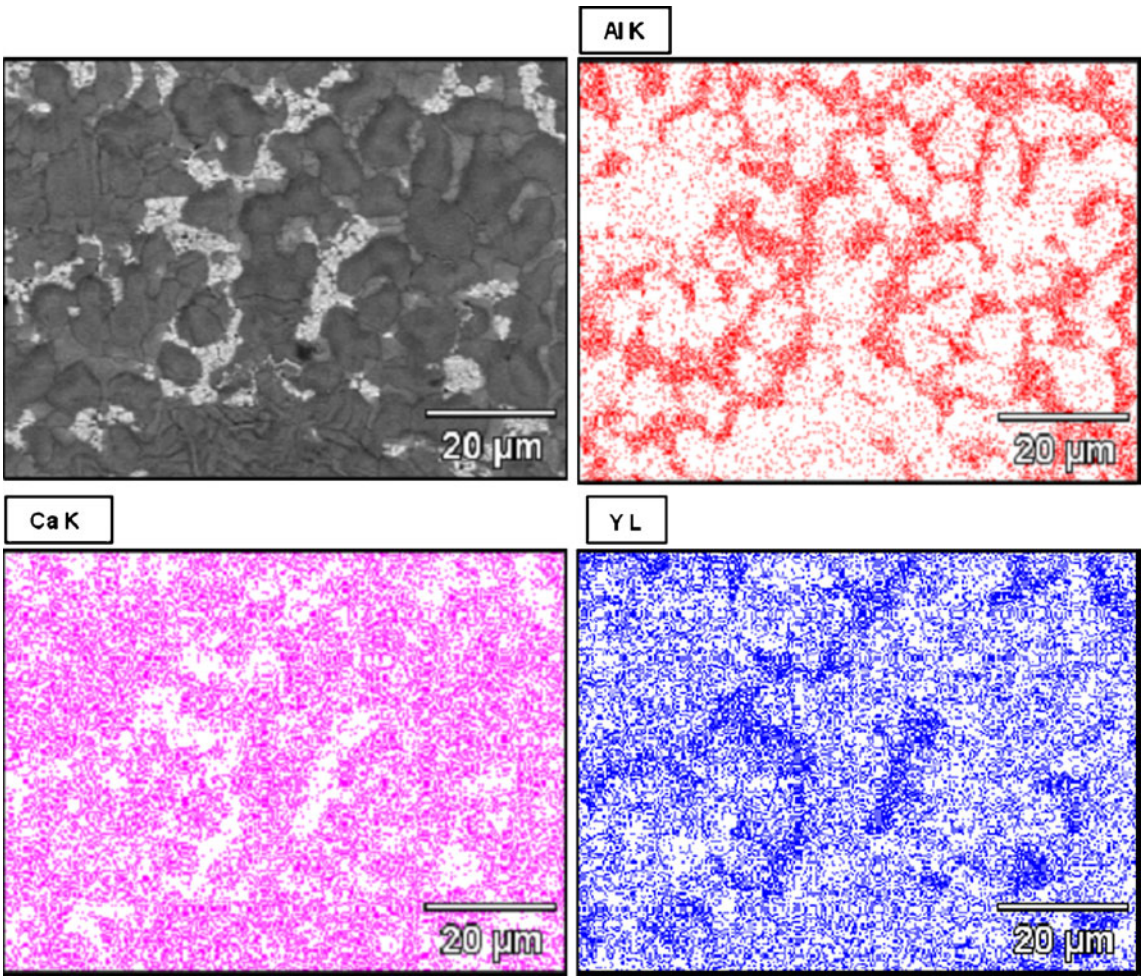

Fig. 11 EDS maps for the constituent ions together with the backscattered electron image for $Y_{0.82}Ca_{0.18}AlO_{3-\delta}$ sample

Effect of phase purity and homogeneity on total conductivity

The fall in conductivity of the oxides with $x>0.10$ may be attributed to the formation of secondary phases and lack of homogeneity as already noticed from the X-ray patterns. Microstructural studies were performed to study this behavior further.

Microstructure of undoped yttrium aluminate

The SEM micrograph of undoped yttrium aluminate prepared by the citrate gel route is shown in Fig. 7. The micrograph shows irregular, predominantly agglomerated grains. This may be attributed to the poor sinterability of the material.

Microstructure of Ca-doped yttrium aluminate

Figure 8 shows the SEM micrographs of $Y_{0.88}Ca_{0.12}AlO_{3-\delta}$. It is seen that the grains are more defined and uniform. The average grain size is about 1.5 μm. The (b) micrograph reveals the presence of a secondary phase which illustrates that the dissolution limit of CaO in $YAlO_3$ is attained at this composition. In order to analyze the fall in conductivity for $x>0.10$, the SEM micrographs of $Y_{0.82}Ca_{0.18}AlO_{3-\delta}$ have been recorded. Figure 9 shows the micrographs of $Y_{0.82}Ca_{0.18}AlO_{3-\delta}$ sample taken in the secondary electron and backscattered electron modes. The secondary electron image reveals distinct grains and grain boundaries which are larger as compared to $Y_{0.88}Ca_{0.12}AlO_{3-\delta}$. The backscattered image reveals regions of different contrasts corresponding to the different phases. The secondary phase grains are much larger than the matrix grains, and some of them take up a distinct elongated shape. EDS microanalysis studies and EDS mapping studies have been performed to analyze the phases qualitatively. EDS microanalysis revealed regions rich in Ca and Al as correlated by the mapping studies as shown in Figs. 10 and 11. The formation of the phase rich in calcium may be due to the presence of excess calcium in the system, and the phase may be $CaAl_4O_7$ as correlated with the XRD data. The grains of this phase are predominantly rod-like, and the reason may be necking of alumina as this is an alumina-rich phase. The other secondary phase formed in traces may be $CaYAlO_4$. The average grain size of this phase is about 3–4 μm. An inverse relationship between conductivity and grain size exists. The grain size of the secondary phase plays a crucial role in the conductivity enhancement process. As the secondary-phase grain size increases, the matrix–secondary phase interface area decreases. As a result, the volume fraction of the regions with locally enhanced conductivity decreases dramatically, leading to an overall decrease in conductivity. The increased dopant concentration affects the crystal lattice, leading to the introduction of geometrical asymmetry. This may be attributed as one of the reasons for the decrease in conductivity. The decrease in the number of mobile oxygen ions due to the formation of oxygen ion vacancy clusters at higher dopant levels may also be attributed as a reason for the decrease in conductivity. The formation of these secondary phases and the increase in grain size of the secondary phase with the increase in the dopant concentration may also be responsible for the fall in conductivity.

Conclusions

The undoped and calcium-doped yttrium aluminate system has been synthesized by the citrate gel and solid-state route, respectively. Single-phase oxides were successfully synthesized for Ca-containing compositions up to $x=0.12$. The electrical conductivity of the system improves on doping with calcium. Maximum conductivity of about 1 mS/cm at 800 °C is obtained for $x=0.10$. The improvement in conductivity may be attributed to the creation of oxide ion vacancies on doping with calcium. With further increase in x, the conductivity falls gradually. The fall in conductivity may be attributed to the formation of secondary phases due to excess levels of calcium as correlated by the SEM data. This work reports $YAlO_3$ as a new family of fast ion conductors. So far, the interpretation that the total conduction is predominantly oxide ionic is a supposition. Further work will be done to investigate the predominant conduction mechanisms in the material.

References

1. Sammells AF, Cook RL, White JH, Osborne JJ, MacDuff RC (1992) Solid State Ion 52:111
2. Kendall KR, Navas C, Thomas JK, Loye HC (1995) Solid State Ion 82:215
3. Vasylechko L, Matkovskii A, Savytskii D, Suchocki A, Wallrafen F (1999) J Alloys Compd 291:57
4. Fergus JW (2006) J Power Sources 162:30
5. Ramadass N (1978) Mater Sci Eng 36:231
6. Stambouli AB, Traversa E (2002) Renew Sustain Energy Rev 6:433
7. Molenda J (2006) Mater Science-Pol 24:5
8. Badwal SPS, Ciacchi FT (2000) Ionics 6:1
9. Steele BCH (2001) Nature 414:345
10. Haile SM (2003) Acta Mater 51:5981
11. Singhal SC, Kendall K (2004) High-temperature solid oxide fuel cells: fundamentals, design and applications. Elsevier Science, The Netherlands
12. Norby T (1999) Solid State Ion 125:1
13. Nowick AS, Du Y (1995) Solid State Ion 77:137
14. Schober T (2003) Solid State Ion 162–163:277
15. Bonanos N (2001) Solid State Ion 145:265
16. Nowick AS, Du Y, Liang KC (1999) Solid State Ion 125:303
17. Iwahara H (1992) Solid State Ion 52:99
18. Cook RL, Sammells AF (1991) Solid State Ion 45:311

19. Knight KS, Bonanos N (1995) Mater Res Bull 30:347
20. Iwahara H, Uchida H, Tanaka S (1983) Solid State Ion 9–10:1021
21. Sammes N, Phillips R, Smirnova A (2004) J Power Sources 134:153
22. Matsumoto H, Nomura I, Okada S, Ishihara T (2008) Solid State Ion 179:1486
23. Gorbova E, Maragou V, Medvedev D, Demin A, Tsiakaras P (2008) J Power Sources 181:207
24. Slade RCT, Singh N (1993) Solid State Ion 61:111
25. Bonanos N, Ellis B, Knight KS, Mahmood M (1989) Solid State Ion 35:179
26. Cervera RB, Oyama Y, Miyoshi Y, Kobayashi K, Yagi T, Yamaguchi S (2008) Solid State Ion 179:236
27. Davies RA, Islam MS, Gale JD (1999) Solid State Ion 126:323
28. Fukui T, Ohara S, Kawatsu S (1999) Solid State Ion 116:331
29. Hayashi H, Inaba H, Matsuyama M, Lan NG, Dokiya M, Tagawa H (1999) Solid State Ion 122:1
30. Huang K, Goodenough JB (2000) J Alloys Compd 303–304:454
31. Huang K, Tichy RS, Goodenough JB (1998) J Am Ceram Soc 81:2576
32. Kato H, Kudo T, Naito H, Yugami H (2003) Solid State Ion 159:217
33. Lybye D, Bonanos N (1999) Solid State Ion 125:339
34. He H, Huang X, Chen L (2001) Electrochim Acta 46:2871
35. Nguyen TL, Dokiya M (2000) Solid State Ion 132:217
36. Nguyen TL, Dokiya M, Wang S, Tagawa H, Hashimoto T (2000) Solid State Ion 130:229
37. Anderson PS, Marques FMB, Sinclair DC, West AR (1999) Solid State Ion 118:229
38. Ishihara T, Matsuda H, Bustam MA, Takita Y (1996) Solid State Ion 86–88:197
39. Ishihara T, Matsuda H, Mizuhara Y, Takita Y (1994) Solid State Ion 70–71:234
40. Yasuda H, Ohnaka I, Mizutani Y, Waku Y (2001) Sci Technol Adv Mater 2:67
41. Kilner JA (1983) Solid State Ion 8:201
42. Takahashi T, Iwahara H (1971) Energy Convers 11:105
43. Alcock CB, Fergus JW, Wang L (1992) Solid State Ion 51:291
44. Kilner JA, Barrow P, Brook RJ, Norgett MJ (1978) J Power Sources 3:67
45. Lybye D, Poulsen FW, Mogensen M (2000) Solid State Ion 128:91
46. Nomura K, Tanase S (1997) Solid State Ion 98:229
47. Takeda Y, Imanishi N, Kanno R, Mizuno T, Higuchi H, Yamamoto O, Takano M (1992) Solid State Ion 53–56:748
48. Tsuji T, Ohashi Y, Yamamura Y (2002) Solid State Ion 154–155:541
49. Sinha A, Sharma BP, Gopalan P (2006) Electrochim Acta 51:1184
50. Cockayne B (1985) J Less-Common Met 114:199
51. Diehl R, Brandt G (1975) Mater Res Bull 10:85
52. Medraj M, Hammondb R, Parvez MA, Drewc RAL, Thompson WT (2006) J Eur Ceram Soc 26:3515
53. Harada M, Goto M (2006) J Alloys Compd 408–412:1193
54. Bauerle JE (1969) J Phys Chem Solids 30:2657
55. Chen TY, Pan RY, Fung KZ (2008) J Phys Chem Solids 69:540
56. Shannon RD (1976) Acta Crystallogr A 32:751